Journal of Advanced Ceramics
2024, **13**(1): 53–62
https://doi.org/10.26599/JAC.2024.9220835

Research Article

High strength mullite-bond SiC porous ceramics fabricated by digital light processing

Jian Sun[1], Jingde Zhang[1,2], Xu Zhang[1], Zihe Li[3], Jianzhang Li[4], Sijie Wei[1,5], Weibin Zhang[1], Weili Wang[1], Guifang Han[1,✉]

[1] *Key Laboratory for Liquid-Solid Structural Evolution and Processing of Materials* (*Ministry of Education*), *School of Materials Science and Engineering*, *Shandong University*, *Jinan 250061*, *China*
[2] *Key Laboratory of Special Functional Aggregated Materials*, *Ministry of Education*, *Shandong University*, *Jinan 250100*, *China*
[3] *Materials and Structures Research Centre*, *Department of Mechanical Engineering*, *University of Bath*, *Bath BA2 7AY*, *UK*
[4] *National Engineering Research Centre of Ceramic Matrix Composite Manufacture Technology*, *Xi'an Golden Mountain Ceramic Composites Co.*, *Ltd.*, *Xi'an 710118*, *China*
[5] *School of Physics and Materials Science*, *Changji University*, *Changji 831100*, *China*

Received: September 20, 2023; Revised: November 11, 2023; Accepted: November 27, 2023

Abstract: Fabricating SiC ceramics via the digital light processing (DLP) technology is of great challenge due to strong light absorption and high refractive index of deep-colored SiC powders, which highly differ from those of resin, and thus significantly affect the curing performance of the photosensitive SiC slurry. In this paper, a thin silicon oxide (SiO_2) layer was *in-situ* formed on the surface of SiC powders by pre-oxidation treatment. This method was proven to effectively improve the curing ability of SiC slurry. The SiC photosensitive slurry was fabricated with solid content of 55 vol% and viscosity of 7.77 Pa·s (shear rate of 30 s^{-1}). The curing thickness was 50 μm with exposure time of only 5 s. Then, a well-designed sintering additive was added to completely convert low-strength SiO_2 into mullite reinforcement during sintering. Complex-shaped mullite-bond SiC ceramics were successfully fabricated. The flexural strength of SiC ceramics sintered at 1550 ℃ in air reached 97.6 MPa with porosity of 39.2 vol%, as high as those prepared by spark plasma sintering (SPS) techniques.

Keywords: digital light processing (DLP); SiC ceramics; pre-oxidation; mullite-bond SiC; mechanical properties

1 Introduction

Due to the advantages of high strength/hardness, high thermal conductivity, low thermal expansion coefficient, and excellent temperature/corrosion/wear resistance [1–5], silicon carbide (SiC) ceramics are widely used in many fields including thermal insulating, filter, catalyst carriers, biology, and aerospace [6–10]. These excellent properties of SiC ceramics are due to a strong Si–C covalent bond. However, this results in difficulty in sintering. In addition, the high strength and hardness of the SiC ceramics make it difficult to machine or process [11,12], which limits the complexity of SiC components and therefore their applications.

As a novel concept, the additive manufacturing technology can realize direct fabrication of complex structure ceramics without machining [13]. Among a range of additive manufacturing techniques, since the digital light processing (DLP) technique has high precision and relatively fast production speed, DLP has been widely applied in the fabrication of complex ceramic components [14–17]. The mechanism of photocuring is based on the polymerization of the photosensitive resin under the irradiation of specific wavelengths of ultraviolet (UV) light [18,19]. In the first step, ceramic powders are added to this photosensitive resin to form uniformly dispersed ceramic slurry. Then, the slurry is cured layer by layer with UV light exposure, and simultaneously ceramic particles are wrapped inside the cured layer to form the designed shape. The DLP technique has been successfully applied in the printing of Al_2O_3 [20–22], ZrO_2 [23], and other oxide ceramics. However, deep-colored SiC has strong light absorption and a refractive index much higher than that of resin. This seriously reduces the penetration depth of light, and the amount of light that can be utilized by photosensitive resin, thereby decreasing the curing thickness of SiC slurry [24].

To solve this problem, researchers decreased the solid content of SiC inside the slurry and/or increased the particle size of SiC powders [24,25]. However, the sample fabricated with low-solid-content slurry showed large shrinkage after the remove of polymer agents, which induced defects and thus poor mechanical properties of the sintered samples. In addition, the large particle size of SiC also resulted in low strength of fabricated parts. Another method to increase the curing thickness of the SiC slurry is to coat shell materials with low absorbance on the surface of SiC particles by physical or chemical methods. As a result, the shell layer can reduce the absorbance and improve curing ability [26–29]. Interestingly, high-temperature oxidation treatment of the SiC powders in air can generate *in-situ* SiO_2 shell layers with low absorbance, which has been proven to increase the curing depth of the SiC slurry [26,27].

However, SiO_2 has low mechanical properties and undergoes phase change during the cooling process accompanied by volume changes. The mismatch of the thermal expansion coefficient (CTE) between cristobalite SiO_2 and SiC ($CTE_{cristobalite}$ =

✉ Corresponding author.
E-mail: gfhan@sdu.edu.cn

0.5×10^{-6} ℃$^{-1}$, $CTE_{SiC} = 4.9\times10^{-6}$ ℃$^{-1}$) [30] results in weak bonding between them and therefore the poor performance of the SiC ceramics. All these factors limit mechanical strength of the printed SiC components. In our previous work [31], we sintered SiC porous ceramics at 1550 ℃ in air with the strength comparable to that fabricated from the spark plasma sintering (SPS) technique. The oxidation-derived SiO_2 from SiC at high temperatures in air was converted into high-strength mullite bonding phases and whisker reinforcement due to the rational design of the composite sintering additives. In the $Al(OH)_3$–Y_2O_3–CaF_2 composite additive, $Al(OH)_3$ provides an Al_2O_3 source to consume SiO_2, and Y_2O_3 promotes the liquid mass transfer and the formation reaction of mullite, while CaF_2 introduces gaseous mass transfer and enhances the formation of mullite whiskers. By converting low-strength SiO_2 to the mullite bond phase and introducing mullite whisker reinforcement, this technique has been proven to effectively enhance mechanical properties of the SiC ceramics.

Therefore, in this study, fine SiC powders with an average particle size of 5.28 μm were pre-oxidized to form a thin SiO_2 shell. The curing depth of the thus fabricated photosensitive slurry was significantly increased, and complex-shaped SiC components were successfully fabricated. SiO_2 was completely converted to mullite by carefully adjusting the added amount of $Al(OH)_3$–Y_2O_3–CaF_2 sintering additives. The fabricated mullite-bond SiC ceramics achieved high flexural strength comparable to that fabricated by the SPS method. This work therefore provides a feasible strategy to enhance the curing ability of the SiC slurry and the mechanical property of sintered SiC at the same time, such that we hope to excite the whole society to realize a low-cost and precise photo-polymerization fabrication of complex-shaped deep-colored ceramic materials such as SiC and Si_3N_4.

2 Experimental

2.1 Materials

Commercial SiC ceramic powders (purity 99.9%, d_{50} = 5.288 μm, Nangong Ruiteng Alloy Material Co., Ltd., China) were chosen as raw materials. Aluminum hydroxide ($Al(OH)_3$, purity 99.9%, average particle size of 10 μm, Aladdin Chemical Co., Ltd., China), yttria (Y_2O_3, purity 99.9%, average particle size of 1 μm, Aladdin Chemical Co., Ltd., China), and calcium fluoride (CaF_2, purity 99.9%, average particle size of 1 μm, Shanghai Maclin Biochemical Technology Co., Ltd., China) were used as sintering additives. Tetramethyl ammonium hydroxide aqueous solution (TMAH, 25 wt%, AR, Aladdin Chemistry Co., Ltd., China) was used as the dispersant (1.6 wt% of ceramic powders). Photosensitive resin used in this paper was commercial resin containing monomers and photoinitiators. The photoinitiator was 2,4,6-trimethylbenzoyl-diphenyl phosphorus oxide (TPO). The monomer was a dimethacrylate based substance, and the dispersant was KOS110 (Guangzhou Tai Runding New Materials Co., Ltd., China).

2.2 Experimental procedure

The SiC powders were evenly spread into an Al_2O_3 crucible and put into a chamber furnace for pre-oxidation in air atmosphere. The heating rate was 10 ℃/min and dwelled at 1200 ℃ for 2, 4, and 6 h. The pre-oxidized powders were ball milled at 300 r/min for 2 h and then sieved through a 100-mesh sieve.

In our previous work [31], the amount of $Al(OH)_3$ was optimized as 6.4 wt% of that of the SiC powders. The amount of Y_2O_3 was optimized as 1.6 wt% of that of SiC and $Al(OH)_3$ powders. The amount of CaF_2 was optimized as 2.0 wt% of that of the $Al(OH)_3$ powders. Since we implemented pre-oxidation in this study and the debinding process in air also introduced oxidation of SiC, the amount of $Al(OH)_3$ was increased to 10, 12.5, and 15 wt% to completely consume additional SiO_2. Also, the amount of Y_2O_3 and CaF_2 was also increased accordingly. All these powders were put into anhydrous ethanol (analytically pure) to form a suspension with solid loading of 50 vol%, and TMAH was added to the suspension as the dispersant to enhance the mixing uniformity of SiC and additive powders. After ball milling for 4 h with a planetary ball mill at a rotating speed of 300 r/min, the slurry was dried in a vacuum drying oven. In the process of obtaining composite powders by drying, the drying temperature was 90 ℃, and the time was more than 24 h. The dried powders were then crushed and ground through a 100-mesh screen to obtain composite powders.

The composite powders were mixed with commercial photosensitive resin to obtain ceramic slurry with solid loadings of 45, 50, and 55 vol%, and KOS110 (5 wt% of the total weight of ceramic powders) was used as the dispersant agent. After the ceramic slurry was planetary ball milled for 5 h at a rotating speed of 300 r/min, a vacuum drying oven (ZK-025, Shanghai Experimental Instrument Factory, China) was used for deforming of 1 h to obtain uniformly dispersed photocurable ceramic slurry. The temperature of the ceramic slurry in the vacuum defoaming process was controlled at room temperature of about 25 ℃.

The DLP printer (PC5003A-50, Xi'an Dianyun Biotechnology Co., Ltd., China) with a UV light wavelength of 405 nm was used in this study. The intensity of the light source used was 30 mW/cm^2. This instrument used a digital mask device (DMD) with a resolution of 1920 × 1080 pixels. The dot resolution on the printing plane was 50 μm, and the control accuracy in the printing direction was around 10 μm. For the printing parameters, the single layer thickness and the UV light exposure time were set to 50 μm and 3 s, respectively. Printing was conducted layer-by-layer until the designed shape was obtained. Furthermore, within the scope of this investigation, ceramic green bodies were prepared through the printing process and subsequently subjected to sintering to yield the final ceramic products. The heating rate in the debinding process was 1 ℃/min till 600 ℃. After holding for 1 h, the temperature was raised to 1200 ℃ at a rate of 5 ℃/min, and finally to the sintering temperature of 1450, 1500, and 1550 ℃ at a heating rate of 10 ℃/min and holding time of 2 h.

2.3 Characterizations

An X-ray diffractometer (D/max 2500 PC, Rigaku, Japan, Cu Kα, λ = 0.1548 nm) was used to obtain X-ray diffraction (XRD) patterns for sintered ceramic materials. A scanning electron microscope (SEM; JSM-7800, JEOL, Japan) equipped with an energy dispersion spectrometer (EDS) was used to study the microstructure of powders and cross-sections of the sintered ceramic materials. The viscosity of the ceramic slurry was measured by a rotating rheometer (R/S+ Rheometer, Brookfield, USA), and the test temperature was maintained at 25 ℃ using a temperature controller (Brookfield-TC). A square (20 mm × 20 mm) cured single layer was obtained by exposing the SiC slurry inside a glass dish for 5–50 s using the DLP 3D printer digital mask device (DMD). After cleaning and erasing the uncured stock, a digital micrometer (211-101, Dongguan Sanliang Measuring Tools Co., Ltd., China) was used to measure the curing thickness for at least 5 points. The flexural strength was measured in a microcomputer control electronic universal testing machine (4505, Instron Experimental Equipment Trading Co., Ltd., USA)

using a three-point bending test (3PBT) with a loading speed of 0.5 mm/min and a span of 30 mm for at least 5 samples (3 mm × 4 mm × 35 mm). Apparent porosity was determined by Archimedes' drainage hydrostatic method with at least 5 samples.

3 Results and discussion

3.1 Pre-oxidation of SiC powders

The XRD patterns of the raw SiC powders and those after pre-oxidation are shown in Fig. 1(a). The red line presented XRD of the raw materials used in the experiment, which well matched the standard diffraction pattern of 6H–SiC. After the pre-oxidation treatment at 1200 ℃ for 2, 4, and 6 h, the crystal structure of the SiC powders did not change significantly, but a new phase peak at 2θ of around 21.7°, which should be due to the formed cristobalite (SiO_2). A local magnification of the main diffraction peak of the cristobalite phase is shown in Fig. 1(b). It can be seen that the diffraction peak intensity of cristobalite gradually increased with the prolongation of pre-oxidation time. The phase composition change that occurred in the pre-oxidation process was that the SiC powders oxidized in air at high temperatures generating amorphous SiO_2, which crystallized into cristobalite phases during the cooling process as Reactions (1) and (2):

$$SiC + 2O_2 \Rightarrow SiO_2\,(\text{amorphous}) + CO_2 \quad (1)$$

$$SiO_2\,(\text{amorphous}) \Rightarrow SiO_2\,(\text{cristobalite}) \quad (2)$$

The surface morphology of the raw SiC powders and that after pre-oxidation were shown in Fig. 2. The original SiC powders appeared as irregular shapes with relatively smooth surfaces as shown in Fig. 2(a). After pre-oxidation, some tiny particles were observed on the surface of the SiC particles, which might be due to the chalking effect during pre-oxidation or ball milling (Figs. 2(b)–2(d)). The surface of the SiC powders became rougher with increasing the pre-oxidation time.

The element distribution of the SiC raw powders before oxidation is shown in Figs. 3(a)–3(d), where C and Si were the main elements on the surface. After the pre-oxidation treatment (Figs. 3(e)–3(h)), besides C and Si, O was also detected on the surface of the particles. The distribution of elements O and Si was consistent with the profile of particles. Combined with the XRD result in Fig. 1, it could be indicated that a scaly cristobalite layer formed on the surface of the SiC powders after pre-oxidation treatment.

The TEM image of pre-oxidized SiC powders is shown in Fig. 4. A thin layer of SiO_2 was found on the surface of the SiC crystal, and its thickness was about 50–100 nm. The oxide shell layer was non-uniform, which might be caused by the ball milling process. Combined with the XRD results, the oxide layer was cristobalite phase.

As particle size has a great effect on the viscosity of slurries [24],

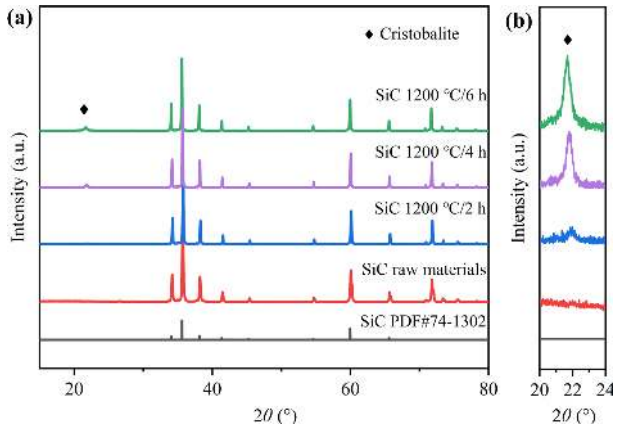

Fig. 1 XRD patterns of raw SiC powders and those after pre-oxidation at 1200 ℃ for different time: (a) overall patterns; (b) local magnification of diffraction peak at 21.7 ° in (a).

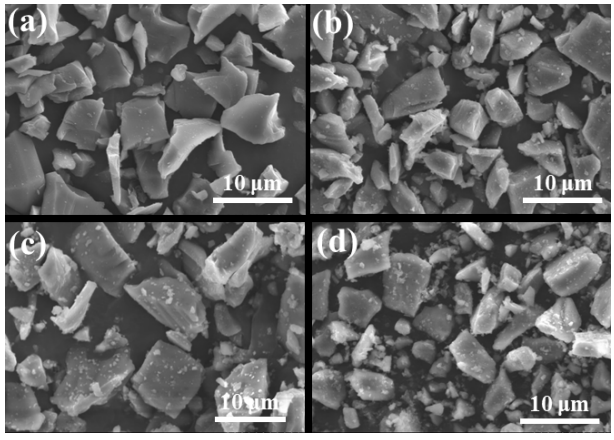

Fig. 2 SEM images of SiC powders before and after oxidation: (a) raw SiC powders before oxidation; SiC powders oxidized at 1200 ℃ for (b) 2 h, (c) 4 h, and (d) 6 h.

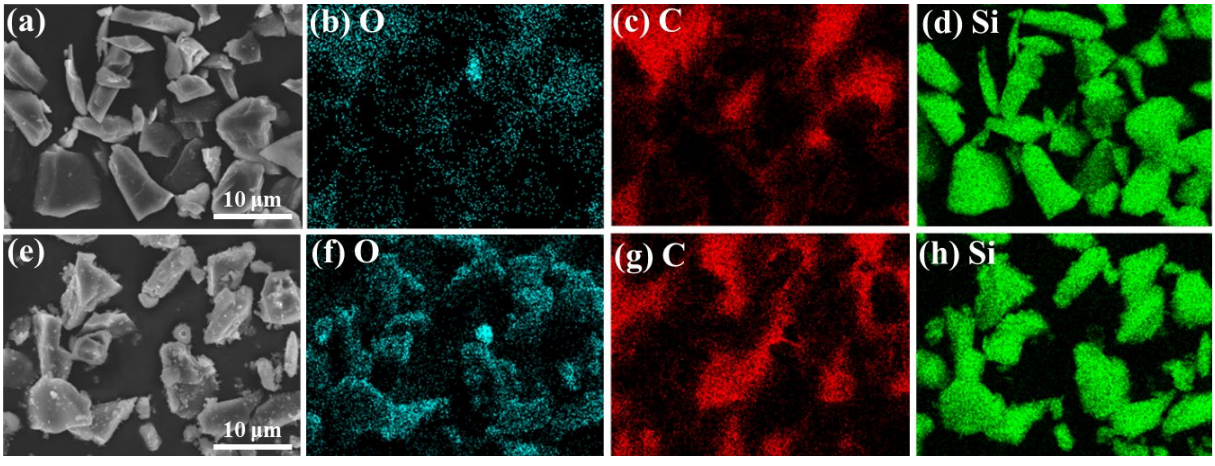

Fig. 3 SEM images and element distribution of SiC powders before and after oxidation: (a) raw SiC powders before oxidation; (e) SiC powders oxidized at 1200 ℃ for 4 h; (b–d) EDS mapping for (a) and (f–h) for (e).

the particle size distribution of SiC powders before and after oxidation at 1200 ℃ for different time was measured and shown in Fig. 5. Pre-oxidized powders were ball milled and then sieved. It can be seen that, d_{50} of raw SiC powders was 5.288 μm, which changed to 4.851, 5.047, and 5.346 μm after oxidation at 1200 ℃ for 2, 4, and 6 h. The variation was quite small. Therefore, it can be concluded that the viscosity of slurry made from SiC powders before and after oxidation is not strongly related to particle size changes.

3.2 Photocuring ability of SiC-based slurry

With experimental verification, it was found that the solid loading of the pure fine SiC powder-based slurry was difficult to reach 35 vol% without additives. That was because the dispersion behavior of the SiC powders inside the photosensitive resin was poor, and the sedimentation of the SiC powders occurred quickly. As a result, the SiC powder-based slurry without additives was not suitable for printing. Herein, the raw SiC powders and pre-oxidized ones were mixed with the sintering additives and added to commercial resin to prepare the photocurable SiC slurry with a solid content of 45 vol%. The curing ability of the slurry was now discussed.

The curing layer thickness of the SiC ceramic slurry varied with the exposure time of UV light as shown in Fig. 6. For the slurry fabricated from raw SiC powders, no obvious curing/polymerization occurred until the UV light exposure time was above 20 s. With the increase in the exposure time, the curing layer thickness increased. When the exposure time reached 45 s, the curing layer thickness was around 46 μm. For the slurry with pre-oxidized SiC powders, the curing performance was greatly

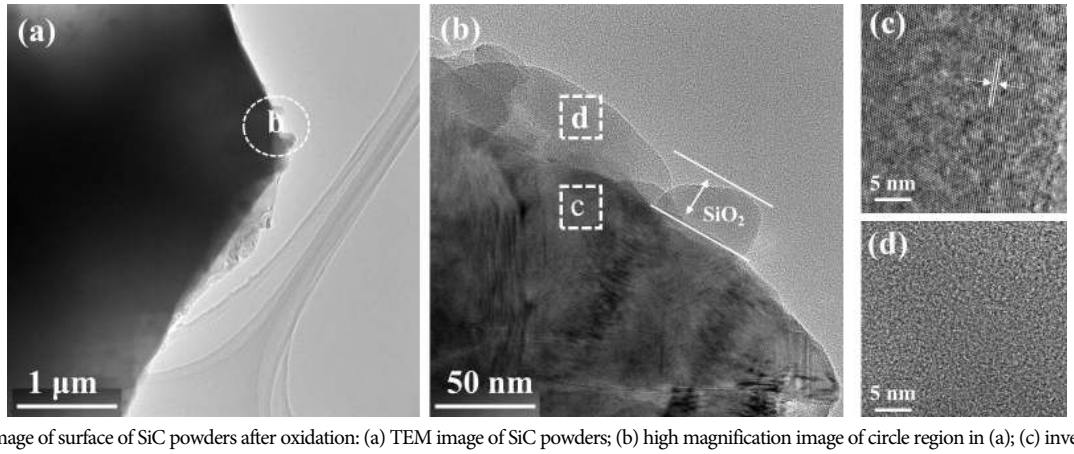

Fig. 4 TEM image of surface of SiC powders after oxidation: (a) TEM image of SiC powders; (b) high magnification image of circle region in (a); (c) inverse fast Fourier transform pattern of area in (b); (d) inverse fast Fourier transform pattern of area in (b).

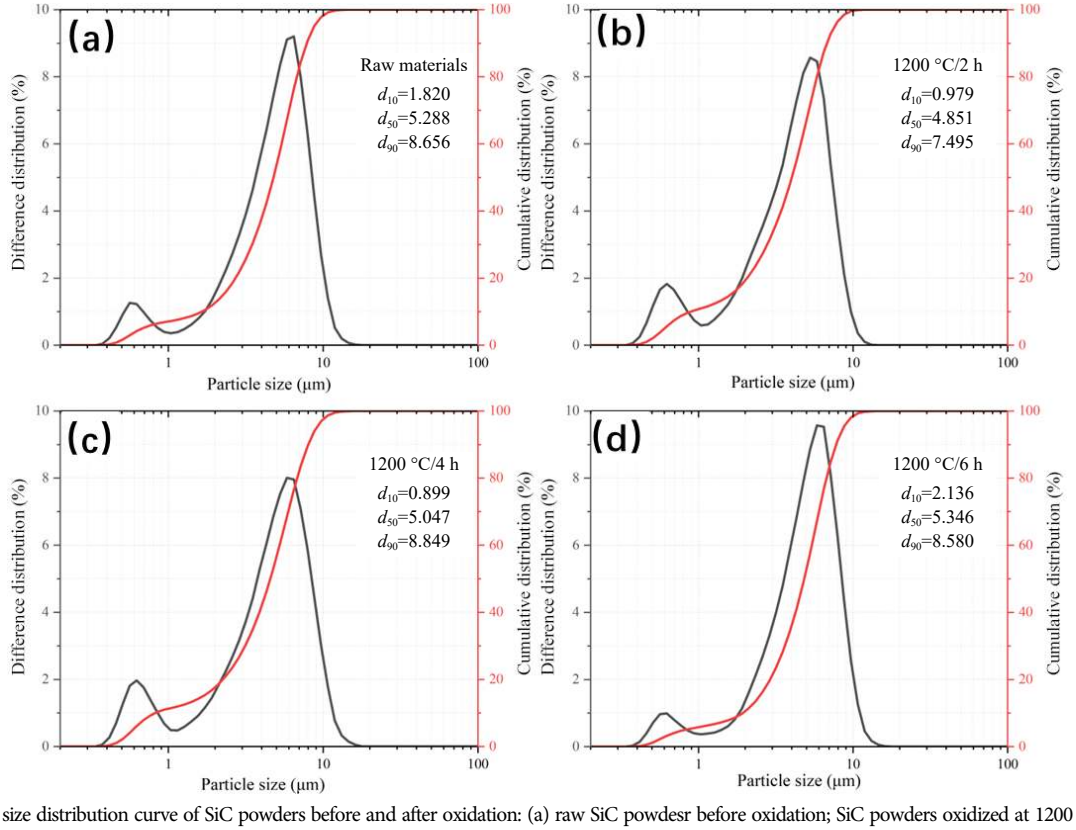

Fig. 5 Particle size distribution curve of SiC powders before and after oxidation: (a) raw SiC powdesr before oxidation; SiC powders oxidized at 1200 ℃ for (b) 2 h, (c) 4 h, and (d) 6 h.

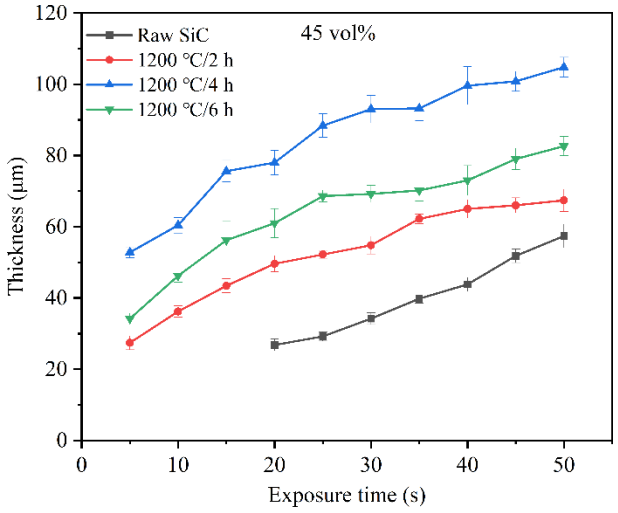

Fig. 6 Curve between curing thickness of SiC ceramic slurry with exposure time for raw SiC powders and pre-oxidized SiC powders at 1200 ℃ for different time.

improved. Much shorter exposure time was required to obtain the same curing thickness compared to the raw SiC powder-based slurry. Among them, the ceramic slurry with the SiC powders treated at 1200 ℃ for 4 h achieved the highest curing thickness at all the range of the tested exposure time. To be specific, this slurry exhibited a curing thickness as high as 51 μm with exposure time of only 5 s, which was 40 s shorter than that of the control group. As a result, the improved curing layer thickness can fully meet the requirement for photocuring 3D printing, and therefore the printing efficiency. According to the existing reports, the slurry with un-treated SiC powders exhibited a curing thickness of < 30 μm with exposure time of 90 s [24], whose exposure time is twice while the curing thickness is thinner than that of the raw SiC powder-based slurry in this work. In Ref. [27], 4.32 μm-sized SiC powders were pre-oxidized at 1300 ℃, and the fabricated slurry showed a curing thickness of 59 μm with exposure time of 5 s, which was comparable with that of the treated SiC powder-based slurry in this work.

With the extension of the oxidation time, the thickness of the oxide layer on the SiC surface would increase, and the curing ability of the ceramic slurry would be improved. This was consistent with other reports [27].

The influence of the pre-oxidation time on curing properties of the ceramic slurry exhibited a non-linear trend, i.e., at the same exposure time, the curing layer thickness first increased with the pre-oxidation time increasing from 2 to 4 h, and decreased with the pre-oxidation time further increasing to 6 h. To explore the influencing factors, the viscosity of the four ceramic slurry at the solid loading of 45 vol% was tested as shown in Fig. 7(a). It can be clearly seen that the pre-oxidation treatment effectively reduced the viscosity of the SiC slurry. Among them, the slurry with the 1200 ℃/4 h treated SiC powders showed the highest viscosity in the whole testing range of the shear rate. The viscosity values at the shear rate of 30 s^{-1} are shown in Fig. 7(b). For the raw SiC powder-based slurry, the viscosity was 2.543 Pa·s. For the slurry made from the powders pre-oxidized at 1200 ℃ for 2, 4, and 6 h, the viscosity decreased to 0.997, 1.369, and 0.859 Pa·s, respectively.

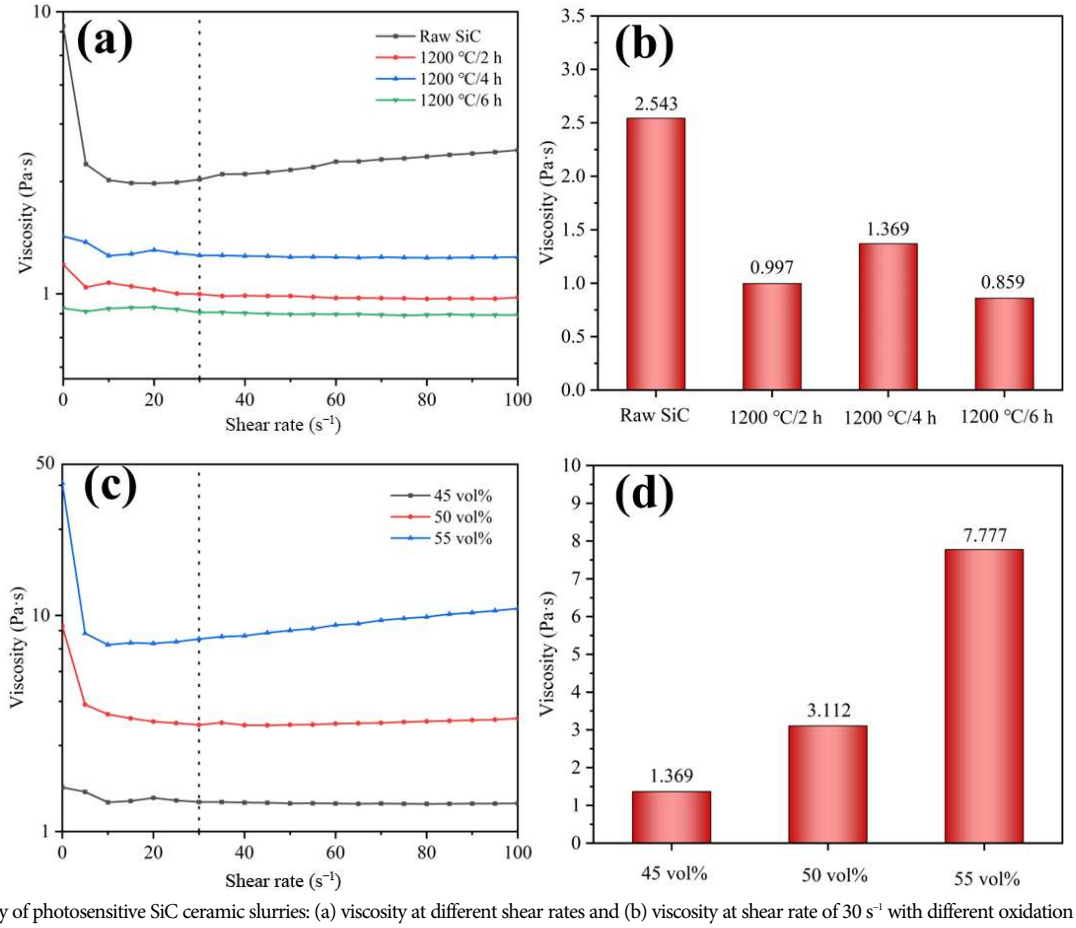

Fig. 7 Viscosity of photosensitive SiC ceramic slurries: (a) viscosity at different shear rates and (b) viscosity at shear rate of 30 s^{-1} with different oxidation time and fixed solid content of 45 vol%; (c) viscosity at different shear rates and (d) the viscosity at shear rate of 30 s^{-1} of slurry with different solid loadings prepared with SiC powders pre-oxidized at 1200 ℃ for 4 h.

Effects of the solid loading on the viscosity of the ceramic slurry fabricated from 4 h pre-oxidized SiC were further studied, and the results are shown in Figs. 7(c) and 7(d). When the solid loading increased from 45 to 50 vol%, the viscosity of the slurry slightly increased from 1.369 to 3.112 Pa·s. With the solid loading further increasing to 55 vol%, the viscosity of the slurry was still less than 10 Pa·s at a shear rate of 30 s^{-1}, which is a criterion to judge whether the slurry is suitable for printing [32]. To date, The viscosity of the slurry with a pre-oxidized SiC particle size of 10 μm exceeded 10 Pa·s at a shear rate of 30 s^{-1} in a 55 vol% solid content [26]. However, there have been few reports of the SiC slurry with high solid loadings and low viscosity using powders with a particle size of around 5 μm.

To investigate the effect of sintering additives on the viscosity, three slurry were prepared separately as shown in Fig. 8. The slurry A contained only pre-oxidized SiC powders. Based on this, $Al(OH)_3$ was added to form the slurry B. Also, in the slurry C, along with pre-oxidized SiC powders, all additives, including $Al(OH)_3$, Y_2O_3, and CaF_2 were added. When the solid load of the slurry A reached 45 vol%, it showed a paste-like consistency with a complete loss of flowability. Poor flowability was observed when the solid content was 40 vol%. To facilitate the test, the solid content of the slurry A was decreased to 35 vol%. The solid content of 45 vol% was fabricated for the slurry B and C to maintain the consistency with the above result.

As shown in Fig. 8(a), a strong shear-thinning behavior was observed for the slurry A. The viscosity of both slurry B and C almost became constant when the shearing rate was higher than 20 s^{-1}. The viscosity of these slurry at a shear rate of 30 s^{-1} was shown in Fig. 8(b). The visocisity of the slurry A was 1.375 Pa·s, which changed to 2.232 and 1.369 Pa·s with the addition of $Al(OH)_3$ and $Al(OH)_3$+Y_2O_3+CaF_2, respectively. Considering the lower solid content of the slurry A, we can conclude that the addition of additives has a small effect on their viscosity.

Considering the best curing ability of the slurry made from the 1200 ℃/4 h treated SiC powders and also the acceptable viscosity of the slurry at a solid loading of 50 vol%, this slurry was used to print SiC bodies in the following work. To validate the feasibility of using the slurry to print complex structures, a range of models were designed, and printed, and sintered, as shown in Fig. 9. Complex shapes were successfully maintained after sintering. The result proved that the combination of pre-oxidation with the addition of sintering additives was an effective way to enhance the curing ability of the SiC slurry. The line shrinkage was similar for the *x*- and *y*-axes in the horizontal direction with an average shrinkage of 12.5%, and 22.7% for the *z*-axis along the print direction. The total volume shrinkage was 41%.

The roughness of the top surface and side surface along the print direction of the green body were measured and shown in Fig. 10. The average surface roughness (R_a) of these two surfaces was less than 1 μm, indicating the smooth feature of printing surfaces.

The surface microstructure of the green body is shown in Fig. 11. The top surface of the green body is distributed with particles, and no obvious defects such as bumps and dents were observed (Figs. 11(a) and 11(b)). In the side surface along the printing direction, as shown in Figs. 11(c) and 11(d), printing layers were observed without any other visible defects. The locally enlarged image in Fig. 11(d) demonstrated that the combination between layers was good, and there was no obvious layering boundary and no debonding.

The top surface microstructure of the sintered body is shown in Figs. 12(a) and 12(b). There were many pore structures distributed on the top surface, and obvious rod-like grains were observed around the pores. The particles were bonded together through the glass phase, and no obvious crack defects were observed. On the side surface along the printing direction, as shown in Figs. 12(c) and 12(d), wave-like features were observed inheriting the layer-by-layer printing characteristic. No interlayer debonding was noticed from the locally enlarged image in Fig. 12(d).

3.3 Properties of printed SiC ceramics

To avoid the negative impacts of the cristobalite phase generated by pre-oxidation and oxidative debinding/sintering on the performance of the SiC ceramics, $Al(OH)_3$ was added as the Al_2O_3 source to react with SiO_2 and form mullite, as illustrated in Reactions (3) and (4):

$$2Al(OH)_3 \Rightarrow 2Al_2O_3 + 3H_2O \quad (3)$$

$$3Al_2O_3 + 2SiO_2 \Rightarrow 3Al_2O_3 \cdot 2SiO_2\ (\text{mullite}) \quad (4)$$

In addition, Y_2O_3 and CaF_2 were added to enhance the formation of mullite and the length/diameter ratio of the formed mullite reinforcement. Based on the dry pressing process in our previous work, the optimal amount of $Al(OH)_3$ was 6.4 wt% of the weight of SiC powders. However, the debinding treatment in air was required for ceramics printed by the DLP method due to a large amount of addition of organic matter such as photosensitive resin and binders, which prolonged the entire oxidation process. Besides, the SiC powders were also pre-oxidized before making

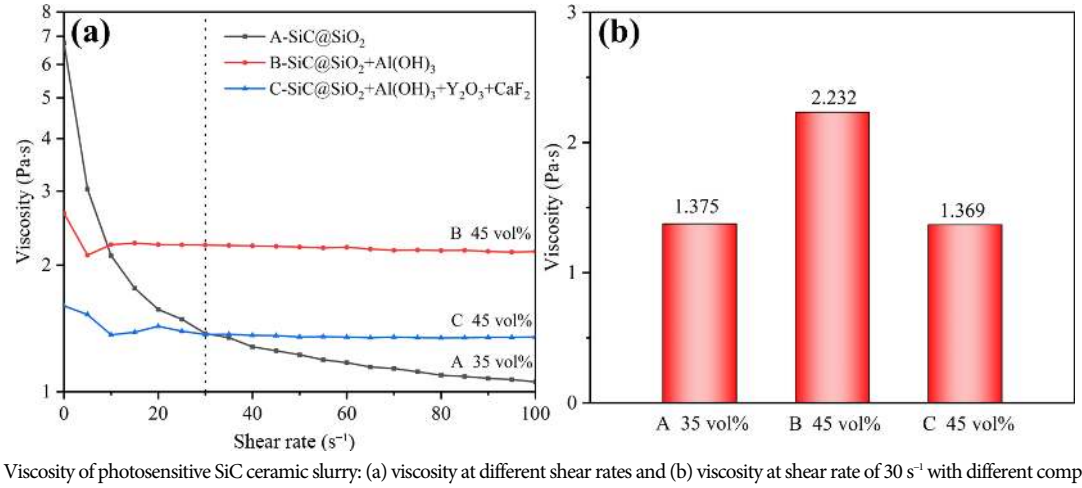

Fig. 8 Viscosity of photosensitive SiC ceramic slurry: (a) viscosity at different shear rates and (b) viscosity at shear rate of 30 s^{-1} with different compositions.

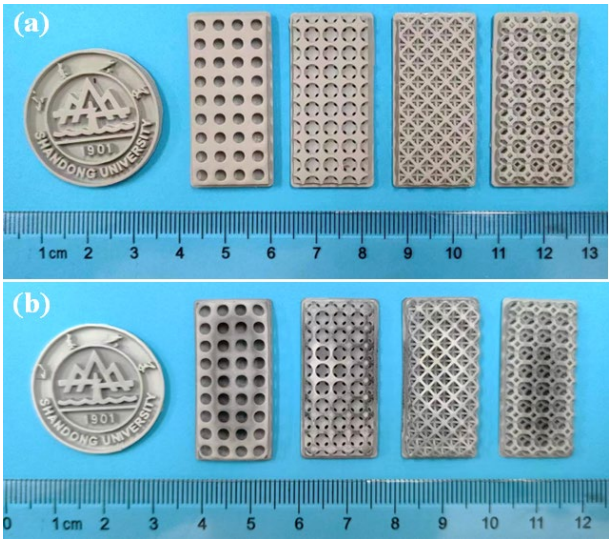

Fig. 9 Photograph of complex structural SiC (a) green bodies and (b) sintered bodies printed by DLP 3D printing.

the slurry. Therefore, it was necessary to explore and adjust the proportion of the sintering additives to completely convert the cristobalite phase into the mullite phase.

In this paper, four different amounts of $Al(OH)_3$, i.e., 6.4, 10, 12.5, and 15 wt%, were added into samples, and their phase composition after sintering was shown in Fig. 13. The crystalline phase of the sintered samples included 6H–SiC, cristobalite, and mullite as shown in Fig. 13(a). With the increase of the $Al(OH)_3$ amount, the diffraction peak of the mullite phase was enhanced and reached the highest when $Al(OH)_3$ was 15 wt%, indicating that some cristobalite continued to react with the Al_2O_3 source. The peak intensity of the cristobalite phase first increased with the $Al(OH)_3$ amount increasing from 6.4 to 10 wt%, and then disappeared at the $Al(OH)_3$ amount of 12.5 wt%. Therefore, the cristobalite produced in the whole process was completely consumed at the $Al(OH)_3$ amount of 12.5 wt%.

Interestingly, at the amount of $Al(OH)_3$ to 15 wt%, a tiny diffraction peak of the cristobalite phase reappeared. Since the cristobalite phase has been eliminated at the $Al(OH)_3$ addition amount of 12.5 wt%, $Al(OH)_3$ should be excessive. However, no diffraction peaks of Al_2O_3 were detected in the XRD result, indicating that the Al_2O_3 source had been consumed. Therefore, it could be inferred that the excessive addition of $Al(OH)_3$ might accelerate the oxidation of SiC and therefore produce an extra amount of the cristobalite phase [31,33], in which further investigation is expected in the future.

Effects of the sintering temperature on the phase composition of the SiC ceramic materials with 12.5 wt% $Al(OH)_3$ addition were shown in Fig. 13(b). With the increase of the sintering temperature, the intensity of the diffraction peak of the cristobalite phase decreased gradually, indicating that the higher sintering temperature enhanced the entire mullitization process. Theoretically, at a lower sintering temperature of 1450 ℃, the content of cristobalite produced by oxidation during sintering should be less than that at 1550 ℃, since a higher temperature induces severer oxidation of SiC. However, as shown in Fig. 13(b), a larger amount of the cristobalite phase was observed for the SiC ceramic materials sintered at 1450 ℃ compared to that sintered at 1550 ℃. This was mainly because the sintering temperature of 1450 ℃ was not high enough to enable the mullite formation reaction to completely conduct. As a result, increasing the sintering temperature enhanced the formation reaction of mullite and therefore the elimination of the cristobalite phase. As shown in Fig. 13(b), with the increase of the sintering temperature, the intensity of the diffraction peaks of mullite increased while that of the cristobalite phase decreased. The cristobalite phase was out of detection when the sintering temperature reached 1550 ℃. In summary, the optimal addition amount of $Al(OH)_3$ and sintering temperature were found to be 12.5 wt% and 1550 ℃, respectively, at which, oxidation-derived cristobalite was completely converted into mullite phase, realizing mullite-bonded SiC ceramic fabrication.

The microstructure and element distribution at the cross section of the sintered SiC ceramic materials are shown in Fig. 14. Although they were porous, the particles were bonded together,

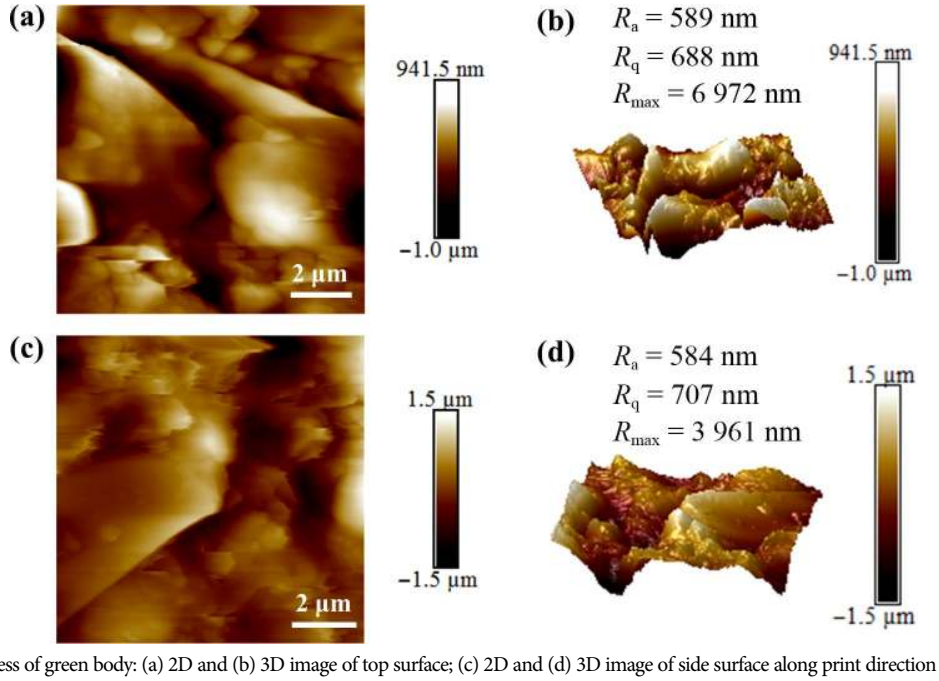

Fig. 10 Surface roughness of green body: (a) 2D and (b) 3D image of top surface; (c) 2D and (d) 3D image of side surface along print direction where R_a is the average roughness, R_q is the root-mean-square deviation, and R_{max} is the maximum roughness depth.

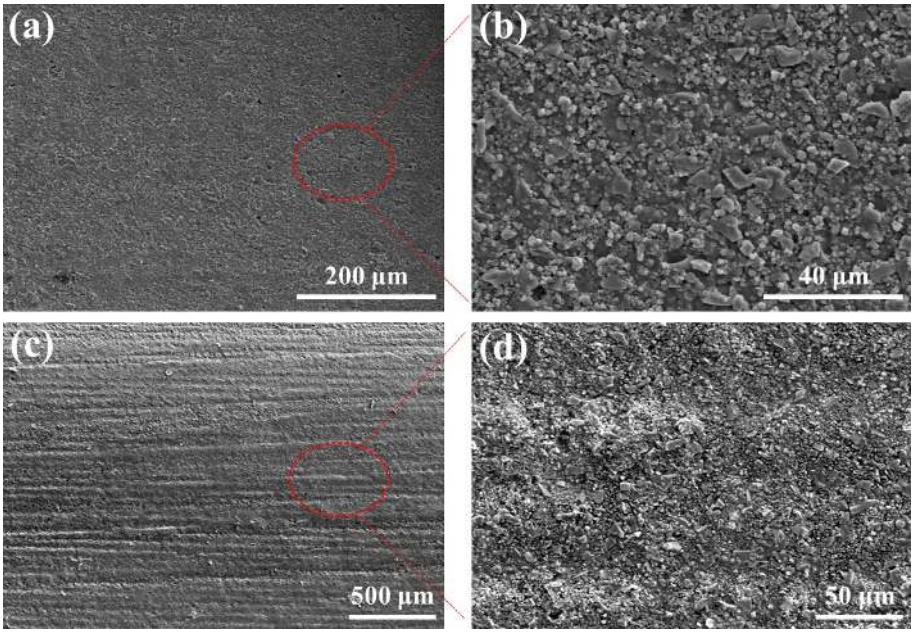

Fig. 11 SEM images of printed green body: (a, b) top surface and (c, d) side surface in *z*-axis printing direction.

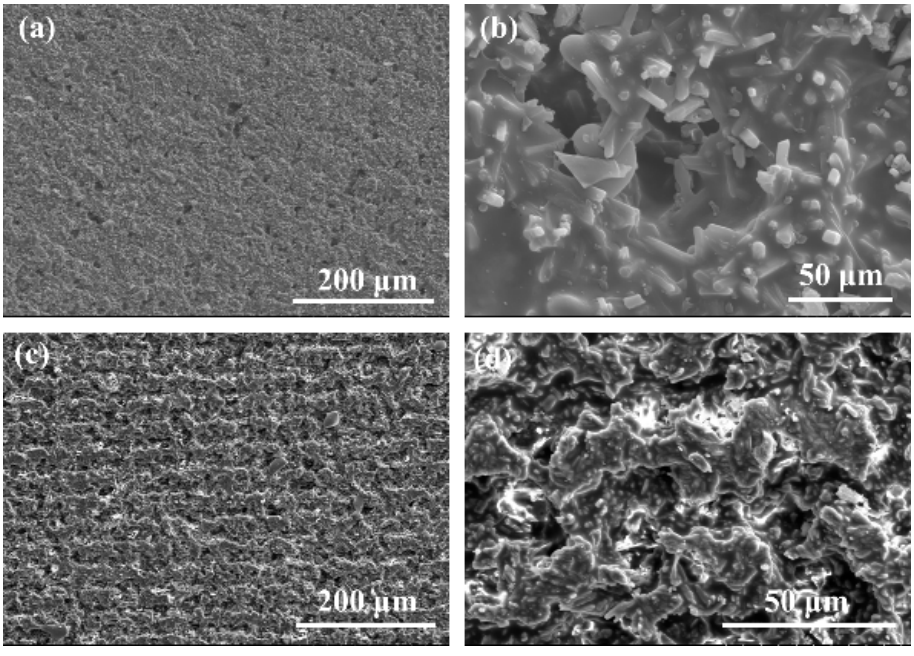

Fig. 12 SEM images of sintered ceramic body: (a, b) top surface and (c, d) side surface in *z*-axis printing direction.

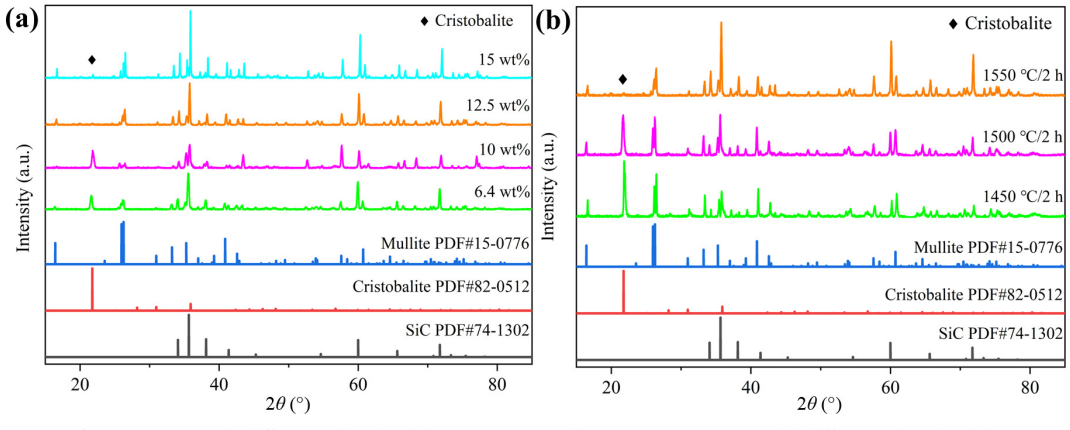

Fig. 13 XRD patterns of SiC ceramics with different $Al(OH)_3$ addition amounts and sintering temperatures: (a) different $Al(OH)_3$ addition amounts sintered at 1550 ℃/2 h; (b) different sintering temperatures with 12.5 wt% $Al(OH)_3$ addition.

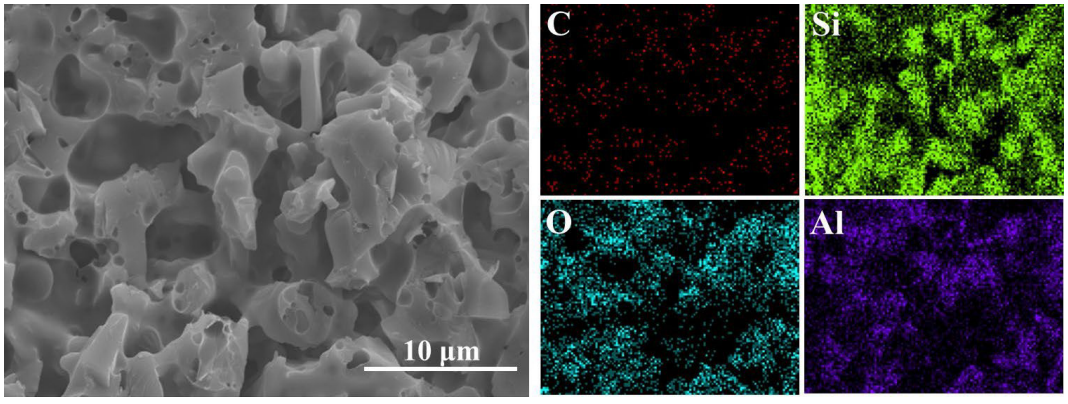

Fig. 14 Micromorphology and element distribution of cross section of sintered SiC ceramic materials.

and no loose individual SiC particles were observed. According to the EDS mapping result, Si, O, and Al elements were distributed uniformly. This suggested that the mullite phase was formed as a bonding phase between SiC particles making the materials well sintered. The low sintering temperature of 1550 ℃ in air can also effectively reduce the fabrication cost of complex SiC components compared to the traditional high temperature/pressure and vacuum/atmosphere sintering processes.

The flexural strength and apparent porosity of the SiC ceramic materials sintered at 1550 ℃ in air by the DLP process were shown in Fig. 15. The average flexural strength reached 97.6 MPa, and the apparent porosity was 39.2 vol%. For comparison, the performances of the SiC ceramic materials fabricated by other techniques in literature, including the flexural strength and porosity, were collected and listed in Table 1. The flexure strength achieved in this study was 94.8% higher than that sintered at 2000 ℃ (50.1 MPa) in an Ar atmosphere by the DLP process, whose porosity information remained unclear [27]. In addition, the excellent flexural strength achieved by the DLP process in this work was also comparable to that fabricated by other techniques, e.g., SPS [34] and dry pressing method in our previous work [31] with similar porosity, and much higher than the SiC ceramic materials fabricated by dry pressing and sintering from other groups.

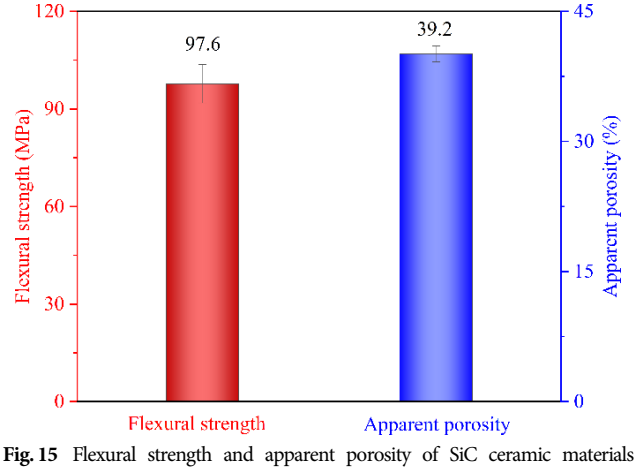

Fig. 15 Flexural strength and apparent porosity of SiC ceramic materials sintered at 1550 ℃ in air by DLP technique.

The flexural strength of SiC porous ceramics prepared in this study was high compared to the sintered bodies with similar apparent porosity, but high porosity was a limitation to the ceramics' properties. The density of sintered ceramics could be improved by subsequent post-treatment processes, such as PIP, CVI, and RMI techniques, to enhance their properties [8,35–38]. Ding *et al.* [8] and Chen *et al.* [37] greatly enhanced the density and strength of SiC and C/SiC by PIP post-treatment [8,37]. Other researchers combined PIP with CVI [36,38] or CVI with RMI [35], and the properties of SiC-based composites were greatly enhanced. These treatments provided practical ideas for our future research.

4 Conclusions

In this paper, complex-shaped SiC ceramic materials with high flexural strength were successfully fabricated by the DLP technique and low-temperature and air-atmosphere sintering. With the pre-oxidation treatment, SiO_2 shell layers formed on the SiC powders. As a result, the printing ability of the SiC photosensitive slurry was effectively enhanced even though the SiC particle size was as fine as 5 μm: a high curing thickness was achieved above 50 μm with exposure time as short as 5 s; the viscosity of the SiC slurry with a solid loading of 55 vol% was as low as 7.77 Pa·s at a shear rate of 30 s^{-1}. Moreover, with the rational design of the sintering additives, the oxidation-derived cristobalite in the materials was completely consumed and

Table 1 Comparison of apparent porosity and flexural strength of SiC porous ceramics prepared by photocuring and traditional methods

Material; additive	Process	Sintering condition	Flexural strength (MPa)	Apparent porosity (vol%)	Ref.
SiC; $Al(OH)_3$+Y_2O_3+CaF_2	DLP	Pressureless, 1550 ℃, air	**97.6**	**39.2**	**This work**
SiC	DLP	Pressureless, 2000 ℃, argon	47.9	—	[27]
SiC; Y_2O_3+Al_2O_3	SLA	Pressureless, 1950 ℃, nitrogen	229.0	10.2	[39]
SiC	—	SPS, 1800 ℃, vacuum	103.0	35.7	[34]
SiC; MoO_3+Al_2O_3	Dry pressing	Pressureless, 1000 ℃, air	66.0	45.4	[40]
SiC; $Al(OH)_3$+Y_2O_3+CaF_2	Dry pressing	Pressureless, 1550 ℃, air	113.0	40.3	[31]
SiC; fly ash+MoO_3	Dry pressing	Pressureless, 1000 ℃, air	38.4	36.4	[41]
SiC; Al_2O_3+graphite	Dry pressing	Pressureless, 1450 ℃, air	27.5	44.4	[42]

converted into a higher-strength mullite bonding phase. The thus fabricated SiC ceramic materials exhibited flexural strength of 97.6 MPa at apparent porosity of 39.2 vol%, which is comparable to that fabricated by the SPS process. This work therefore provides a novel method to fabricate DLP-process SiC ceramic materials with excellent printing ability and high mechanical strength.

Acknowledgements

This work was supported by Shandong University–MSEA International Institute for Materials Genome Joint Innovation Center for Advanced Ceramics, and the Key Research and Development Projects of Shaanxi Province (Nos. 2018ZDCXL-GY-09-06 and 2021ZDLGY14-06).

Declaration of competing interest

The authors have no competing interests to declare that are relevant to the content of this article.

References

[1] Naslain R, Guette A, Rebillat F, *et al.* Boron-bearing species in ceramic matrix composites for long-term aerospace applications. *J Solid State Chem* 2004, **177**: 449–456.
[2] Zhang JX, Huang R, Gu H, *et al.* High toughness in laminated SiC ceramics from aqueous tape casting. *Sciptar Mater* 2005, **52**: 381–385.
[3] Yuan SW, Yang ZC, Chen GB. 3D microstructure model and thermal shock failure mechanism of a Si_3N_4-bonded SiC ceramic refractory with SiC high volume ratio particles. *Ceram Int* 2019, **45**: 4219–4229.
[4] Liu JX, Tian C, Xiao HN, *et al.* Effect of B_4C on co-sintering of SiC ceramic membrane. *Ceram Int* 2019, **45**: 3921–3929.
[5] Duan WY, Yin XW, Li Q, *et al.* A review of absorption properties in silicon-based polymer derived ceramics. *J Eur Ceram Soc* 2016, **36**: 3681–3689.
[6] Katoh Y, Snead LL, Henager CH Jr, *et al.* Current status and recent research achievements in SiC/SiC composites. *J Nucl Mater* 2014, **455**: 387–397.
[7] Krenkel W, Berndt F. C/C–SiC composites for space applications and advanced friction systems. *Mater Sci Eng A* 2005, **412**: 177–181.
[8] Ding GJ, He RJ, Zhang KQ, *et al.* Stereolithography 3D printing of SiC ceramic with potential for lightweight optical mirror. *Ceram Int* 2020, **46**: 18785–18790.
[9] Katoh Y, Snead LL, Szlufarska I, *et al.* Radiation effects in SiC for nuclear structural applications. *Curr Opin Solid State Mater Sci* 2012, **16**: 143–152.
[10] Padture NP. Advanced structural ceramics in aerospace propulsion. *Nat Mater* 2016, **15**: 804–809.
[11] Rosso M. Ceramic and metal matrix composites: Routes and properties. *J Mater Process Technol* 2006, **175**: 364–375.
[12] Han DY, Mei H, Xiao SS, *et al.* A review on the processing technologies of carbon nanotube/silicon carbide composites. *J Eur Ceram Soc* 2018, **38**: 3695–3708.
[13] Chen Z, Sun XH, Shang YP, *et al.* Dense ceramics with complex shape fabricated by 3D printing: A review. *J Adv Ceram* 2021, **10**: 195–218.
[14] Zhang F, Li ZA, Xu MJ, *et al.* A review of 3D printed porous ceramics. *J Eur Ceram Soc* 2022, **42**: 3351–3373.
[15] Fu YL, Chen ZW, Xu G, *et al.* Preparation and stereolithography 3D printing of ultralight and ultrastrong ZrOC porous ceramics. *J Alloys Compd* 2019, **789**: 867–873.
[16] Hassanin H, Essa K, Elshaer A, *et al.* Micro-fabrication of ceramics: Additive manufacturing and conventional technologies. *J Adv Ceram* 2021, **10**: 1–27.
[17] He RJ, Zhou NP, Zhang KQ, *et al.* Progress and challenges towards additive manufacturing of SiC ceramic. *J Adv Ceram* 2021, **10**: 637–674.
[18] Liu G, Zhang XF, Chen XL, *et al.* Additive manufacturing of structural materials. *Mater Sci Eng R Rep* 2021, **145**: 100596.
[19] Rasaki SA, Xiong DY, Xiong SF, *et al.* Photopolymerization-based additive manufacturing of ceramics: A systematic review. *J Adv Ceram* 2021, **10**: 442–471.
[20] Xing HY, Zou B, Lai QG, *et al.* Preparation and characterization of UV curable Al_2O_3 suspensions applying for stereolithography 3D printing ceramic microcomponent. *Powder Technol* 2018, **338**: 153–161.
[21] An D, Li HZ, Xie ZP, *et al.* Additive manufacturing and characterization of complex Al_2O_3 parts based on a novel stereolithography method. *Int J Appl Ceram Technol* 2017, **14**: 836–844.
[22] Nie GL, Li YH, Sheng PF, *et al.* Microstructure refinement-homogenization and flexural strength improvement of Al_2O_3 ceramics fabricated by DLP-stereolithography integrated with chemical precipitation coating process. *J Adv Ceram* 2021, **10**: 790–808.
[23] Wu HD, Liu W, He RX, *et al.* Fabrication of dense zirconia-toughened alumina ceramics through a stereolithography-based additive manufacturing. *Ceram Int* 2017, **43**: 968–972.
[24] Ding GJ, He RJ, Zhang KQ, *et al.* Stereolithography-based additive manufacturing of gray-colored SiC ceramic green body. *J Am Ceram Soc* 2019, **102**: 7198–7209.
[25] Tang J, Guo XT, Chang HT, *et al.* The preparation of SiC ceramic photosensitive slurry for rapid stereolithography. *J Eur Ceram Soc* 2021, **41**: 7516–7524.
[26] Cao JW, Miao K, Xiong SF, *et al.* 3D printing and *in situ* transformation of SiCnw/SiC structures. *Addit Manuf* 2022, **58**: 103053.
[27] Shi ZA, Wu JM, Fang ZQ, *et al.* Influence of high-temperature oxidation of SiC powders on curing properties of SiC slurry for digital light processing. *J Adv Ceram* 2023, **12**: 169–181.
[28] Brinckmann SA, Patra N, Yao J, *et al.* Stereolithography of SiOC polymer-derived ceramics filled with SiC micronwhiskers. *Adv Eng Mater* 2018, **20**: 1800593.
[29] He RJ, Ding GJ, Zhang KQ, *et al.* Fabrication of SiC ceramic architectures using stereolithography combined with precursor infiltration and pyrolysis. *Ceram Int* 2019, **45**: 14006–14014.
[30] Talwar DN, Sherbondy JC. Thermal expansion coefficient of 3C–SiC. *Appl Phys Lett* 1995, **67**: 3301–3303.
[31] Li ZH, Chang ZX, Liu XR, *et al.* A novel sintering additive system for porous mullite-bonded SiC ceramics: High mechanical performance with controllable pore structure. *Ceram Int* 2022, **48**: 4105–4114.
[32] Zhang KQ, Xie C, Wang G, *et al.* High solid loading, low viscosity photosensitive Al_2O_3 slurry for stereolithography based additive manufacturing. *Ceram Int* 2019, **45**: 203–208.
[33] Ebrahimpour O, Dubois C, Chaouki J. Manufacturing process for *in situ* reaction-bonded porous SiC ceramics using a combination of graft polymerization and sol–gel approaches. *Ind Eng Chem Res* 2014, **53**: 17604–17614.
[34] Zhao PQ, Li QG, Yi RJ, *et al.* Fabrication and microstructure of liquid sintered porous SiC ceramics through spark plasma sintering. *J Alloys Compd* 2018, **748**: 36–43.
[35] Li JX, Liu YS, Nan BY, *et al.* Microstructure and properties of C/SiC–diamond composites prepared by the combination of CVI and RMI. *Adv Eng Mater* 2019, **21**: 1800765.
[36] Liu RJ, Wang F, Zhang JP, *et al.* Effects of CVI SiC amount and deposition rates on properties of SiC_f/SiC composites fabricated by hybrid chemical vapor infiltration (CVI) and precursor infiltration and pyrolysis (PIP) routes. *Ceram Int* 2021, **47**: 26971–26977.
[37] Chen YF, Zhang L, Zhao YN, *et al.* Mechanical behaviors of C/SiC pyramidal lattice core sandwich panel under in-plane compression. *Compos Struct* 2019, **214**: 103–113.
[38] Ortona A, Donato A, Filacchioni G, *et al.* SiC–SiC_f CMC manufacturing by hybrid CVI–PIP techniques: Process optimisation. *Fusion Eng Des* 2000, **51–52**: 159–163.
[39] Wang KJ, Liu RZ, Bao CG. SiC paste with high curing thickness for stereolithography. *Ceram Int* 2022, **48**: 28692–28703.
[40] Xing ZH, Hu YH, Xiang DP, *et al.* Porous SiC–mullite ceramics with high flexural strength and gas permeability prepared from photovoltaic silicon waste. *Ceram Int* 2020, **46**: 1236–1242.
[41] Das D, Nijhuma K, Gabriel AM, *et al.* Recycling of coal fly ash for fabrication of elongated mullite rod bonded porous SiC ceramic membrane and its application in filtration. *J Eur Ceram Soc* 2020, **40**: 2163–2172.
[42] Ding SQ, Zhu SM, Zeng YP, *et al.* Effect of Y_2O_3 addition on the properties of reaction-bonded porous SiC ceramics. *Ceram Int* 2006, **32**: 461–466.